Nanoscale

PAPER

View Article Online
View Journal | View Issue

Cite this: *Nanoscale*, 2014, **6**, 13544

Optimized performances of tetrapod-like ZnO nanostructures for a triode structure field emission planar light source

Yiren Chen,[a] Liqin Hu,[b] Hang Song,*[a] Hong Jiang,[a] Dabing Li,*[a] Guoqing Miao,[a] Zhiming Li,[a] Xiaojuan Sun,[a] Zhiwei Zhang[a] and Tailiang Guo*[b]

Received 25th July 2014,
Accepted 7th September 2014

DOI: 10.1039/c4nr04235b

www.rsc.org/nanoscale

Tetrapod-like ZnO (T-ZnO) nanostructures were synthesized by a simple vapor phase oxidation method without any catalysts or additives. We optimized the performances of T-ZnO nanostructures by adjusting the partial pressure of Zn vapour in the total pressure of the quartz chamber and obtained T-ZnO nanostructure materials of high purity, uniform morphology and size and high aspect ratio with a low turn-on electric field of 2.75 V μm^{-1}, a large field enhancement factor of 3410 and good field emission stability for more than 70 hour continuous emission. Besides, based on the optimized T-ZnO, we developed metal grid mask-assisted water-based electrostatic spraying technology, and fabricated a large-scale, pollution-free, hole-shaped array T-ZnO nanostructure cathode used in a triode structure field emission planar light source. The controllable performances of the triode device were intensively investigated and the results showed that the triode device uniformly illuminated with a luminous intensity as high as 8000 cd m^{-2} under the conditions of 200 V grid voltage and 3300 V anode voltage. The research in this paper will benefit the development of a high performance planar light source based on T-ZnO nanostructures.

Introduction

Due to the chemical stability, wide direct band gap, large exciton binding energy, high aspect ratio and controllable size, zinc oxide (ZnO) nanostructures have been considered to be among the most promising materials for nanoscale electronic and optoelectronic devices.[1] Among various morphologies of ZnO, the tetrapod-like ZnO (T-ZnO) nanostructure has attracted considerable attention. So far, the T-ZnO nanostructure has been extensively investigated in gas sensors,[2,3] ultraviolet (UV) photodetectors,[4–6] field effect transistors,[7] nanoscale logic devices[8] and dye-sensitized solar cells.[9] The intrinsic three-dimensional (3D) spatial structure of T-ZnO with four needle-shaped legs distributing in tetrahedral angles and nanoscale tips is beneficial for application as a cold cathode material in field-emission-based devices such as field emission displays (FEDs), cathodoluminescence and field emission planar light sources, electron microscopes, *etc.*[10] As a matter of fact, many studies on T-ZnO nanostructures as field emitters have been carried out.[11–13] However, the features of T-ZnO nanostructures such as morphology, size, purity and aspect ratio presented a great difference and the field emission often exhibited poor stability due to the effect of adsorbates on T-ZnO nanostructures introduced in the process of transfer.[14] Moreover, the reported structure of the field emission device based on the T-ZnO nanostructure was mainly limited to the simple diode structure which suffered from poor emission uniformity and low luminous efficiency.

In this letter, we first grew T-ZnO nanostructures by a simple controllable vapour phase oxidation method without any catalysts or additives and obtained T-ZnO nanostructure materials of high purity, uniform morphology and size, high aspect ratio and good field emission characteristics by adjusting the partial pressure of Zn vapour in the total pressure of the quartz chamber. Then, the optimized T-ZnO nanostructure materials were transferred to a hole-shaped Ag cathode by the metal grid mask-assisted water-based electrostatic spraying method which was superior to the methods for screen-printing T-ZnO and organic solvent hybrids reported by Lei *et al.*[15] and metal-cation-assisted electrophoretic deposition.[16,17] The screen-printing and electrophoretic deposition methods introduced additives that affected the emission stability. Finally, a field emission planar light source based on the metal grid triode structure was fabricated, which overcame the disadvantages of the simple diode structure and realized practicable, efficient, and uniform lighting. By the *in situ* comparative study of the performance of the triode structure light source,

[a]*State Key Laboratory of Luminescence and Applications, Changchun Institute of Optics, Mechanics and Physics, Chinese Academy of Sciences, 3888 Dongnanhu Road, Changchun 130033, People's Republic of China. E-mail: songh@ciomp.ac.cn, lidb@ciomp.ac.cn*

[b]*College of Physics and Information Engineering, Fuzhou University, 523 Industrial Road, Fuzhou 350002, People's Republic of China. E-mail: gtl@fzu.edu.cn*

we demonstrated that the optimum performance could be obtained by controlling the grid voltage working in the saturation region.

Experimental section

Preparation of T-ZnO nanostructure materials

T-ZnO nanostructures were synthesized by a simple controllable vapour phase oxidation method using a low vacuum horizontal tube furnace. In the process of material preparation, a ceramic plate held with high purity zinc powder (purity: 99.99%) was pre-placed into a quartz tube and the flow rates of Ar and O_2 were adjusted to 200 sccm and 10 sccm, respectively. Before heating, the chamber was pumped to the pressure of 500, 200, 100 and 20 Pa, respectively. Then, the temperature was increased at a rate of 100 °C min^{-1} and kept at 950 °C for 60 min. By changing the chamber pressure so as to adjust the partial pressure of Zn vapour, we obtained different T-ZnO nanostructures at chamber pressures at 500, 200, 100 and 20 Pa, corresponding to samples A, B, C and D, respectively. The effect of the chamber pressure on the morphology of T-ZnO nanostructures could be investigated.

Fabrication of the triode structure field emission device

Ag strip electrodes were used as cathodic electrodes of the triode structure. At first, we obtained periodic hole-shaped array cathodic electrodes by fabricating a hole-shaped insulator layer on Ag electrodes by a thick film screen-printing process and high temperature sintering. Then, T-ZnO nanostructures were dispersed in deionized water by ultrasound and formed a T-ZnO suspension of 0.05 wt%. Using the method of electrostatic spraying, the T-ZnO suspension was transferred to hole-shaped Ag electrodes and dried at 100 °C for 30 min. In the spraying process, a hole-shaped metal grid was used as a mask to ensure that T-ZnO nanostructures were only sprayed in the holes. After finishing the preparation of the T-ZnO field emission cathode, it was combined with the hole-shaped metal grid and fluorescent screen to assemble the triode structure device. The metal grid was directly placed on the insulator layer while the fluorescent screen maintained a space of 500 μm from the metal grid.

Characterization and measurement

The morphology and structure of T-ZnO nanostructures were characterized by scanning electron microscopy (SEM, Hitachi S-4800) and X-ray diffraction (XRD, Bruker D8). The field emission properties of samples A, B, C and D were investigated from current density–electric field (J–E) characteristics in the diode structure and measured under the conditions of 9×10^{-5} Pa vacuum pressure, 3 mm × 3 mm effective field emission area and 200 μm distance between the cathode and the anode. The field enhancement factors (β) of the four samples were calculated using the Fowler–Nordheim (FN) equation. All of the electrical properties, including J–E and electron emission stability (J–T), were characterized using the Agilent testing system. In addition, the parameters and morphology of the hole-shaped dielectric layer in the triode structure were characterized using a step profiler (Vecco Dekatk150).

Results and discussion

Fig. 1 shows a typical XRD pattern of the synthesized T-ZnO nanostructure and its macro-morphology which looks like white cotton. The positions of the XRD peaks corresponding to (100), (002), (101), (102), (110) and (103) planes are well consistent with those of the hexagonal wurtzite-structured ZnO (Joint Committee for Powder Diffraction Standards (JCPDS): card no. 36-1451). Its lattice constants are calculated to be 0.3248 and 0.5205 nm for a- and c-axes, respectively, using the Bragg diffraction equation and lattice constant formula of the hexagonal system[18,19] described as follows:

$$2d_{(hkl)} \sin \theta_{(hkl)} = \lambda \quad (1)$$

and

$$\frac{1}{d^2_{(hkl)}} = \frac{4(h^2 + k^2 + hk)}{3a^2} + \frac{l^2}{c^2} \quad (2)$$

where (hkl) is on behalf of Miller indices, $d_{(hkl)}$ is the interplanar spacing, $\theta_{(hkl)}$ is the angle between the incident X-ray and the (hkl) crystal face and λ (= 0.15406 nm) is the wavelength of X-rays.

The T-ZnO nanostructures with different morphologies are synthesized by adjusting the chamber pressure at 500, 200, 100 and 20 Pa, as shown in Fig. 2(a)–(d). The morphologies of T-ZnO nanostructures change along with the variation of the chamber pressure which mainly lies in the adjustment of the Zn partial pressure.[10,20–22] As per the laws of vacuum,[23] at a

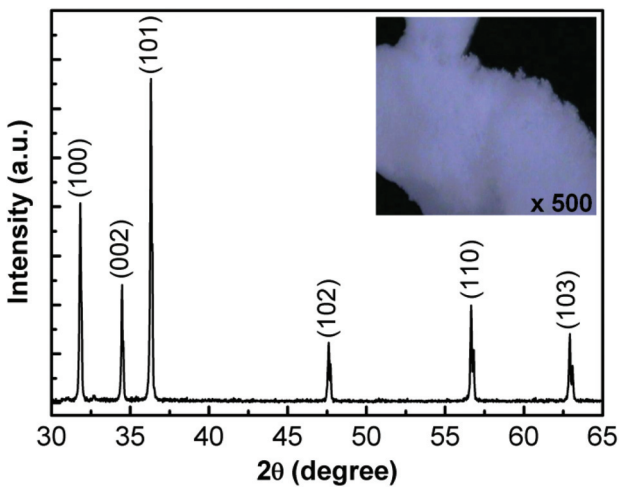

Fig. 1 The typical XRD pattern of the as-grown T-ZnO nanostructure. The inset shows its macro-morphology under a 500 time magnification microscope which looks like cotton.

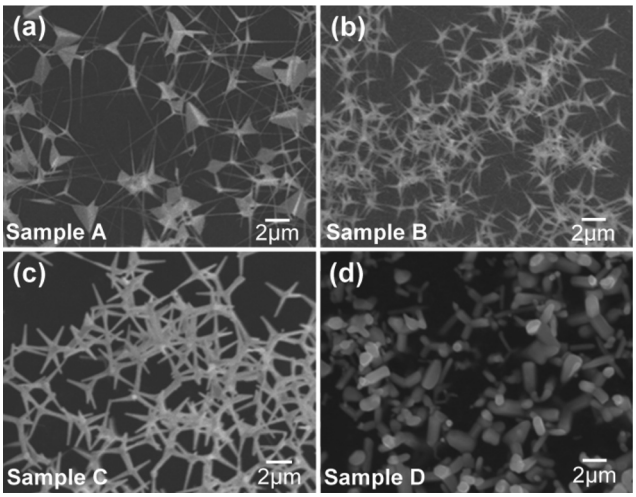

Fig. 2 SEM images of T-ZnO nanostructures under different chamber pressures: (a) 500 Pa, (b) 200 Pa, (c) 100 Pa, and (d) 20 Pa, respectively.

certain temperature, the lower the chamber pressure, the higher is the evaporation rate of Zn, thus resulting in a higher partial pressure of Zn vapour. In contrast, a higher chamber pressure results in a lower partial pressure of Zn vapour. Under high chamber pressure, compared with the low Zn partial pressure, the supply of O_2 is adequate; therefore, the needles of T-ZnO grow enough or even excessively that appear to be butterfly-shaped T-ZnO nanostructures, as shown in Fig. 2(a). With the chamber pressure decrease, the Zn partial pressure increases. In this process, the supply of O_2 undergoes the transition from sufficiency to moderation first, which results in good orientated growth of whiskers and yields T-ZnO nanostructures with uniform morphology and high purity, as shown in Fig. 2(b) and (c). When the chamber pressure further decreases, the partial pressure of O_2 becomes relatively insufficient and cannot meet the need of the whisker growth; this leads to the bad orientated growth of whiskers and generates ZnO particles in the product, as shown in Fig. 2(d). In other words, the T-ZnO nanostructures with uniform morphology can be fabricated at an appropriate Zn partial pressure by well controlling the chamber pressure. In addition, as the partial pressure of Zn vapour increases, the lateral growth of needles of the T-ZnO nanostructure gradually becomes remarkable so that the needles grow thickly. The lateral growth will affect the curvature radius of needles of the T-ZnO nanostructure along with its field enhancement factor.

The field emission properties of samples A, B, C and D are demonstrated in Fig. 3(a) and (b). As shown in Fig. 3(a), different J–E curves are presented. The turn-on electric field (E_{TO}) is conventionally defined as the electric field at the field emission current density of 10 μA cm^{-2}.[24] Therefore, we obtain the E_{TO} of four samples at 3.5 V μm^{-1}, 2.75 V μm^{-1}, 3.9 V μm^{-1} and 7.4 V μm^{-1}, corresponding to samples A, B, C and D, respectively. Moreover, the field emission characteristics can be evaluated using the FN model. According to typical FN

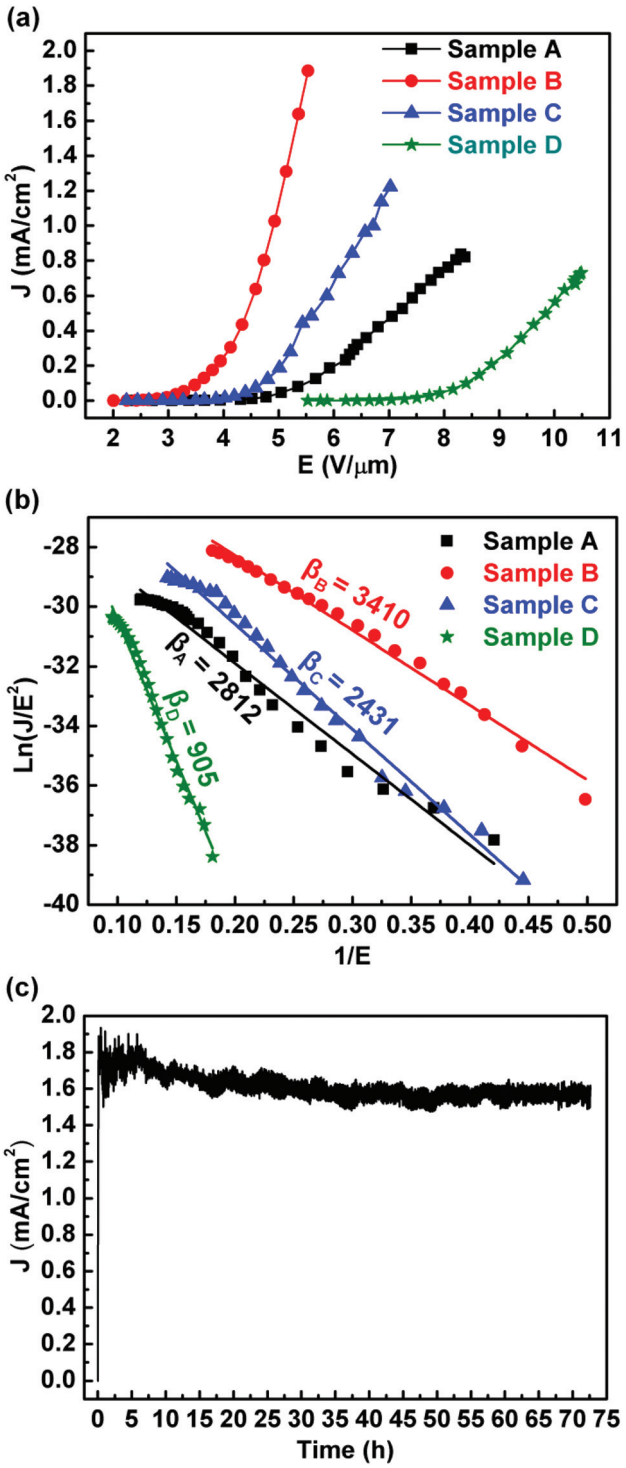

Fig. 3 Field emission properties of samples A, B, C and D: (a) the J–E curves, (b) the corresponding FN plots and (c) the J–T curve of sample B.

theory, the field emission current density J can be described as the equation of electric field E:[10,25–27]

$$J = \frac{A\beta^2 E^2}{\Phi} \exp\left(\frac{-B\Phi^{3/2}}{\beta E}\right) \quad (3)$$

or

$$\ln\frac{J}{E^2} = \ln\frac{A\beta^2}{\Phi} - \frac{B\Phi^{3/2}}{\beta E} \quad (4)$$

where A and B are constants with the values of 1.56×10^{-10} A V^{-2} eV and 6.83×10^3 V $eV^{-3/2}$ μm^{-1}, respectively. Φ is the work function of the material which is 5.3 eV for ZnO.[28] β is the field enhancement factor related to the aspect ratio and curvature radius of needles of T-ZnO nanostructures. By plotting $\ln(J/E^2)$ *versus* $1/E$, we obtain FN plots of four samples, as shown in Fig. 3(b). The observed FN plots exhibit deviation from linearity in a high field region which can be ascribed to the semiconducting nature of T-ZnO involved in the characteristics of the energy band structure and voltage-to-barrier-field conversion factor.[13,27] From the slope of FN plots, the field enhancement factors of the four samples (designated as β_A, β_B, β_C and β_D) are estimated to be 2812, 3410, 2431 and 905, respectively. Sample B presents a higher field enhancement factor due to the advantage of its geometry fabricated at an appropriate Zn partial pressure. Besides, the field emission stability of sample B is also confirmed by J–T measurements, as illustrated in Fig. 3(c). The measurement is carried out at 1100 V for more than 70 h. Its current density undergoes a slight decrease at first, and then turns to stabilization with time. In a word, sample B exhibits excellent characteristics such as uniform morphology and size, low turn-on electric field, large field enhancement factor and good stability which are better than the reported properties of other-shaped ZnO nanostructures[10,29,30] and beneficial for use as a field emitter.

We fabricate a field emission planar light source based on the metal grid triode structure using the T-ZnO nanostructure of sample B as the field emitter. The structural schematic diagram of the triode device is shown in Fig. 4(a). The preparation of the physical device is given in the Experimental section above in detail. Herein, as illustrated in Fig. 4(b), the 500 times magnified microscopy image of the hole-shaped insulator layer is presented. The dimension of the insulator hole is 600 μm for the bottom diameter with a period of 1 mm and the layer thickness is about 12 μm, as measured using a step profiler shown in Fig. 4(d). Fig. 4(c) shows the SEM image of the hole-shaped Ag electrode in the local area. As can be seen, T-ZnO nanostructures with 2 μm long needles are distributed on the surface of the Ag electrode uniformly and uprightly. In addition, the used metal grid has hole-shaped arrays with 600 μm diameter, 1 mm period and 100 μm thickness, as shown in Fig. 4(e).

The performance of the triode structure device is investigated by current–voltage (I–V) under the conditions of 9×10^{-5} Pa vacuum pressure. The electrical connection in the triode structure is shown in the inset of Fig. 5. Fixing the voltage of the anode fluorescent screen (V_A) at 3300 V, we obtained the relationships of anode current (I_A) *versus* grid voltage (V_G), cathode current (I_C) *versus* V_G and grid current (I_G) *versus* V_G by adjusting the V_G from 0 V to 200 V, as shown in Fig. 5. With the increase of V_G, the I_C increases while the I_A undergoes the process of increasing at first, and then tending to saturation. We define four points labelled as a, b, c and d (pointed by green arrows) on the I_A *versus* V_G curve, corresponding to V_G = 0 V, 100 V, 150 V and 200 V, respectively, and record their field emission images in Fig. 6(a)–(d) for *in situ* comparative study. As can be seen from Fig. 6(a), V_G = 0 V which means that the triode device behaves as the diode structure, and the uniformity of luminance is poor. When applying 100 V to V_G, the modulating electric field formed by V_G (about 8.33 V μm^{-1}) slightly improves the uniformity of luminance, as shown in Fig. 6(b). In Fig. 6(c), when V_G is further increased to 150 V, the modulation effect of V_G is obvious that the device emerges large-scale uniform luminance with brightness of 7200 cd m^{-2}. At this point, I_A and I_C increase dramatically. With the further increase of V_G to 200 V, corresponding to the modulating electric field of 16.67 V μm^{-1}, though the luminous intensity still

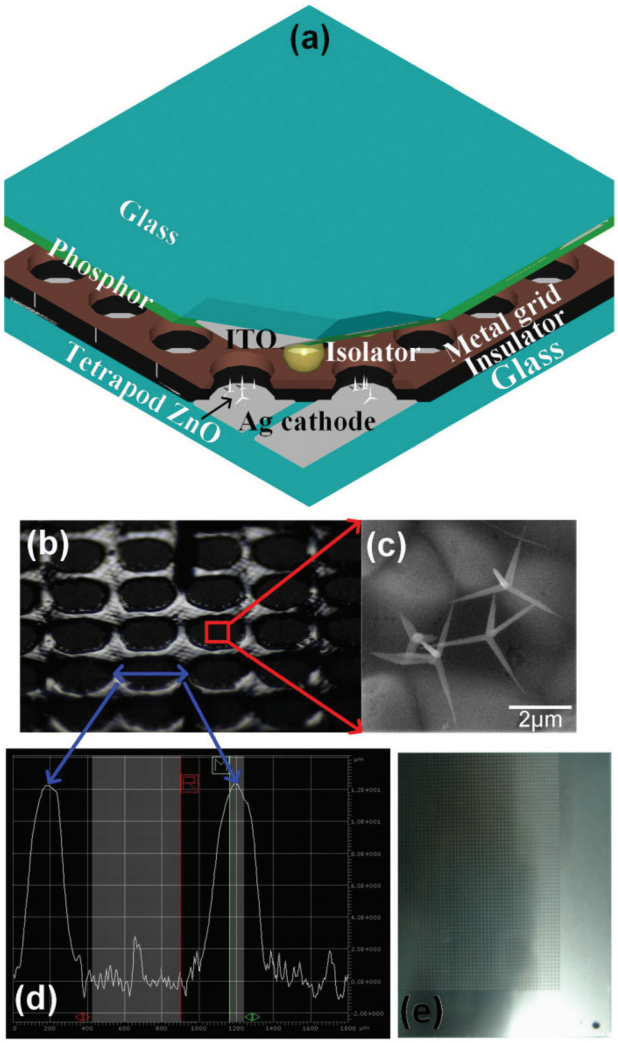

Fig. 4 (a) The structural schematic diagram of the triode device; (b) image of the hole-shaped insulator layer under a 500 time magnification microscope; (c) the SEM image of T-ZnO nanostructures located at the surface of hole-shaped Ag electrodes; (d) the dimension of the insulator hole; (e) the hole-shaped metal grid used in the triode structure.

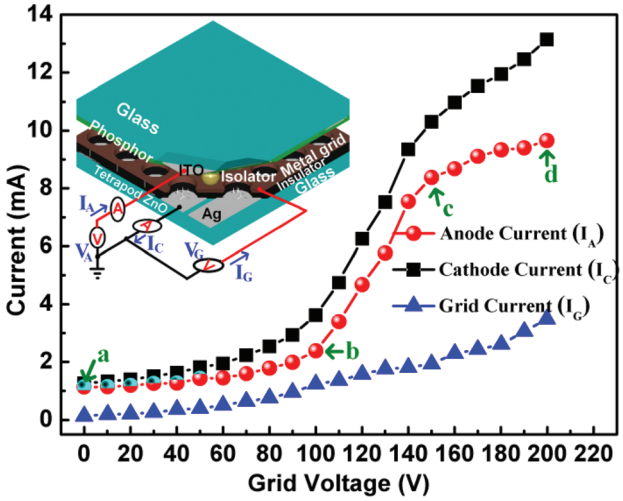

Fig. 5 The relationships of anode current (I_A) *versus* grid voltage (V_G), cathode current (I_C) *versus* V_G and grid current (I_G) *versus* V_G when fixing the anode voltage (V_A) at 3300 V. The inset shows the electrical connection in the triode structure.

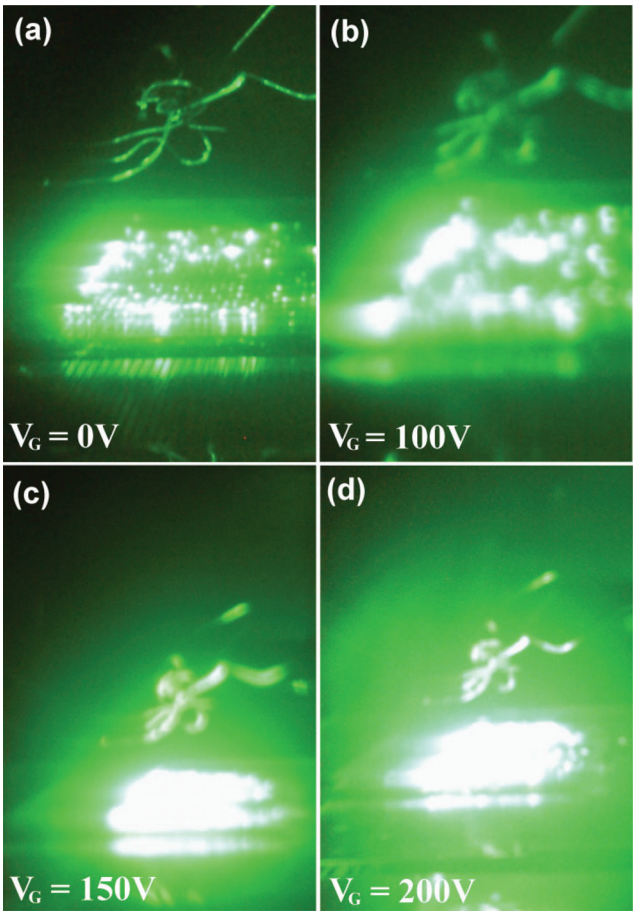

Fig. 6 The field emission images at V_A = 3300 V and (a) V_G = 0 V, (b) V_G = 100 V, (c) V_G = 150 V and (d) V_G = 200 V.

has a certain level enhancement with brightness reaching up to 8000 cd m^{-2} in Fig. 6(d), compared with Fig. 6(c), I_A tends to saturation. However, I_C keeps on increasing in this process. That is to say, the modulation effect of the grid voltage to the anode current has a limit under a specific anode voltage.

The main reason for the saturation of I_A lies in that: with the increase of V_G, the electric field at the tips of T-ZnO nanostructures is enhanced gradually so that more and more electrons will obtain sufficient energy to overcome the barrier of T-ZnO and emit under vacuum to form free electrons. These free electrons move directionally under the accelerating field formed by V_A and generate the cathode current I_C. The I_C can be described as $I_C = I_A + I_G$. When V_G is relatively small, the ability of the metal grid to attract electrons is weak, so the difference between I_A and I_C is not obvious. With the further increase of V_G, when it reaches a certain value (such as 150 V in this paper), although the I_C largely increases, the ability of the metal grid to attract electrons is also enhanced, which weakens the focussing of electron trajectories and captures more and more electrons. Therefore, the I_G substantially increases to restrain the increase of I_A. It results in the saturation of I_A. On the other hand, the weak focussing of electron trajectories leads to relatively large electron beam spots which stimulate the anode fluorescent screen and improve the uniformity of luminance.

Conclusions

By adjusting the partial pressure of Zn vapour in the total pressure of the quartz chamber, T-ZnO nanostructure materials of excellent characteristics were synthesized by a simple vapor phase oxidation method without any catalysts or additives. The optimized T-ZnO nanostructures presented a low turn-on electric field of 2.75 V μm^{-1}, a large field enhancement factor of 3410 and excellent field emission stability for more than 70 h continuous emission, in addition to the uniform morphology and size. Based on the optimized T-ZnO, we developed metal grid mask-assisted water-based electrostatic spraying technology, and fabricated a large-scale, pollution-free, hole-shaped array T-ZnO nanostructure cathode. A triode structure field emission planar light source was assembled using the T-ZnO nanostructure cathode, a hole-shaped metal grid and a fluorescent screen. By the *in situ* comparative study of the performance of the triode structure light source, we demonstrated that the optimum performance could be obtained by controlling the grid voltage working in the saturation region. As the experimental results show, the triode structure light source uniformly illuminated with a luminous intensity as high as 8000 cd m^{-2} under the conditions of 200 V grid voltage and 3300 V anode voltage. It is believed that the research in this paper will benefit the development of a novel, high performance planar light source based on T-ZnO nanostructures.

Acknowledgements

This work was supported by the National Basic Research Program of China (973 Program, grant no. 2010CB327705) and the Jilin Provincial Science & Technology Department (grant no. 20140520116JH).

Notes and references

1 N. Pan, X. P. Wang, K. Zhang, H. L. Hu, B. Xu, F. Q. Li and J. G. Hou, *Nanotechnology*, 2005, **16**, 1069.
2 K. H. Zheng, Y. C. Zhao, K. Deng, Z. Liu, L. F. Sun, Z. X. Zhang, L. Song, H. F. Yang, C. Z. Gu and S. S. Xie, *Appl. Phys. Lett.*, 2008, **92**, 213116.
3 D. Calestani, M. Zha, A. Zappettini, M. C. Carotta, V. Di Natale and L. Zanotti, *Sens. Actuators, B*, 2010, **144**, 472–478.
4 M. C. Newton, S. Firth and P. A. Warburton, *Appl. Phys. Lett.*, 2006, **89**, 072104.
5 Z. X. Zhang, L. F. Sun, Y. C. Zhao, Z. Liu, D. F. Liu, L. Cao, B. S. Zou, W. Y. Zhou, C. Z. Gu and S. S. Xie, *Nano Lett.*, 2008, **8**, 652–655.
6 W. H. Wang, J. J. Qi, Q. Y. Wang, Y. H. Huang, Q. L. Liao and Y. Zhang, *Nanoscale*, 2013, **5**, 5981–5985.
7 Y. D. Gu, J. Zhou, W. J. Mai, Y. Dai, G. Bao and Z. L. Wang, *Chem. Phys. Lett.*, 2010, **484**, 96–99.
8 K. Sun, J. J. Qi, Q. Zhang, Y. Yang and Y. Zhang, *Nanoscale*, 2011, **3**, 2166–2168.
9 R. R. Bacsa, J. Dexpert-Ghys, M. Verelst, A. Falqui, B. Machado, W. S. Bacsa, P. Chen, S. M. Zakeeruddin, M. Graetzel and P. Serp, *Adv. Funct. Mater.*, 2009, **19**, 875–886.
10 F. H. Chu, C. W. Huang, C. L. Hsin, C. W. Wang, S. Y. Yu, P. H. Yeh and W. W. Wu, *Nanoscale*, 2012, **4**, 1471–1475.
11 Q. Wan, K. Yu, T. H. Wang and C. L. Lin, *Appl. Phys. Lett.*, 2003, **83**, 2253–2255.
12 K. Yu, Y. S. Zhang, R. Li Xu, S. X. Ouyang, D. M. Li, L. Q. Luo, Z. Q. Zhu, J. Ma, S. J. Xie, S. H. Han and H. R. Geng, *Mater. Lett.*, 2005, **59**, 1866–1870.
13 A. A. Al-Tabbakh, M. A. More, D. S. Joag, I. S. Mulla and V. K. Pillai, *ACS Nano*, 2010, **4**, 5585–5590.
14 Q. H. Li, Q. Wan, Y. J. Chen, T. H. Wang, H. B. Jia and D. P. Yu, *Appl. Phys. Lett.*, 2004, **85**, 636–638.
15 W. Lei, X. B. Zhang, B. P. Wang, C. G. Lou, Z. Y. Zhu, Z. W. Zhao, C. Li and K. Hou, *IEEE Electron Device Lett.*, 2008, **29**, 452–455.
16 L. M. Yu and C. C. Zhu, *Appl. Surf. Sci.*, 2009, **255**, 8359–8362.
17 Y. Chen, H. Jiang, D. Li, H. Song, Z. Li, X. Sun, G. Miao and H. Zhao, *Nanoscale Res. Lett.*, 2011, **6**, 537.
18 L. Chow, O. Lupan, H. Heinrich and G. Chai, *Appl. Phys. Lett.*, 2009, **94**, 163105.
19 D. Gedamu, I. Paulowicz, S. Kaps, O. Lupan, S. Wille, G. Haidarschin, Y. K. Mishra and R. Adelung, *Adv. Mater.*, 2014, **26**, 1541–1550.
20 Y. H. Leung, A. B. Djurisic, J. Cao, M. H. Xie and W. K. Chan, *Chem. Phys. Lett.*, 2004, **385**, 155–159.
21 G.-H. Lee, *Appl. Surf. Sci.*, 2012, **259**, 562–565.
22 H. Zhang, L. Shen and S. W. Guo, *J. Phys. Chem. C*, 2007, **111**, 12939–12943.
23 A. Roth, *Vacuum Technology*, North-Holland, Amsterdam, 2nd edn, 1982, pp. 400–405.
24 Y. B. Li, Y. Ban and D. Golberg, *Appl. Phys. Lett.*, 2004, **84**, 3603–3605.
25 Y. Sun, H. Cui, L. Gong, J. Chen, P. K. Shen and C. X. Wang, *Nanoscale*, 2011, **3**, 2978–2982.
26 X. B. Yan, B.-K. Tay and P. Miele, *Carbon*, 2008, **46**, 753–758.
27 S. S. Warule, N. S. Chaudhari, J. D. Ambekar, B. B. Kale and M. A. More, *ACS Appl. Mater. Interfaces*, 2011, **3**, 3454–3462.
28 N. S. Ramgir, I. S. Mulla, K. Vijayamohanan, D. J. Late, A. B. Bhise, M. A. More and D. S. Joag, *Appl. Phys. Lett.*, 2006, **88**, 042107.
29 X. M. Qian, H. B. Liu, Y. B. Guo, Y. L. Song and Y. L. Li, *Nanoscale Res. Lett.*, 2008, **3**, 303–307.
30 H. Jiang, J. Q. Hu, F. Gu and C. Z. Li, *Nanotechnology*, 2009, **20**, 055706.